

Modeling fracture in brittle materials with inertia effects using the phase field method

Surya Shekar K. Reddy, Rajagopal Amirtham & Junuthula N. Reddy

To cite this article: Surya Shekar K. Reddy, Rajagopal Amirtham & Junuthula N. Reddy (2023) Modeling fracture in brittle materials with inertia effects using the phase field method, *Mechanics of Advanced Materials and Structures*, 30:1, 144-159, DOI: [10.1080/15376494.2021.2010289](https://doi.org/10.1080/15376494.2021.2010289)

To link to this article: <https://doi.org/10.1080/15376494.2021.2010289>



Published online: 16 Dec 2021.



Submit your article to this journal



Article views: 341



View related articles



View Crossmark data



Citing articles: 1 View citing articles

Modeling fracture in brittle materials with inertia effects using the phase field method

Surya Shekar K. Reddy^a, Rajagopal Amirtham^a, and Junuthula N. Reddy^b 

^aDepartment of Civil Engineering, IIT Hyderabad, Kandi, Sangareddy, Telangana, India; ^bDepartment of Mechanical Engineering, Texas A&M University, College Station, Texas, USA

ABSTRACT

The phase field method uses a length scale parameter to regularize the discrete crack to a diffuse crack, which removes the numerical tracking of the discontinuities in the displacement. The displacement field is coupled with the phase field and both are solved as a sequentially coupled systems using staggered method. The phase field ϕ varies between zero and unity (i.e., $\phi = 0$ for intact region and $\phi = 1$ for fully broken region), and it is a scalar. In this study, a new way of implementation is done using ABAQUS software to solve for the two fields. User defined element subroutine (UEL) is used to solve for the phase field variable and user defined material subroutine (UMAT) for the displacement field variable. Phase field model can simulate any complex crack paths and branching even without previously defined cracks. Some benchmark examples of quasi-static brittle fracture and dynamic brittle fracture are solved and verified with the existing numerical results. To account for the rate-dependent effect under high-rate loading, micro-inertia is incorporated into the phase-field model for dynamic fracture as proposed in the literature and verified with one example.

ARTICLE HISTORY

Received 7 October 2021
Accepted 21 November 2021

KEYWORDS

Phase field method; Abaqus implementation; brittle fracture; hybrid formulation; staggered scheme

1. Introduction

The prediction of failure in structural materials due to crack growth is of great importance in many engineering applications and it led to the increased attention of many researchers to develop several numerical approaches. The original theory on brittle fracture was first proposed by Griffith [1]; then Irwin [2] proposed a new term called the “stress intensity factor” to predict the microscopic plasticity at the crack tip in brittle materials. Both quantified the effect of crack formation based on surface energy term called *the critical energy release rate*. Griffith’s theory can adequately predict the crack propagation but it does not predict crack initiation, branching, or coalescence properly. There are several methods that are currently available which simulate fracture initiation and growth, and they are usually classified as either diffuse or discrete approaches.

In discrete methods such as cohesive surfaces [3], node splitting, and the finite element method [4], the propagation of crack is only between the elements and its path is mesh dependent. The other methods such as extended finite-element method (XFEM) [5], generalized finite-elements method (GFEM) [6], and the phantom-node method [7] the displacement field is enriched. Element erosion technique [8] is another method used to separate the fracture surfaces where the stresses are made zero in the failed elements. The first simulation of crack branching is done by inter-element crack method [9, 10], where a crack is modeled by dividing the element edges.

The cohesive zone models (CZM) are another type of discrete models pioneered by [11, 12] where the formation of crack take place across an extended crack tip called cohesive zone and is restricted by cohesive traction. The traction-separation laws are mimicked by the traction and the displacement jumps across the localization bands. The general softening laws such as linear, exponential, and hyperbolic, can be approximated for traction separation laws for sufficient accuracy.

A graph-based finite element analysis (GraFEA) is presented in [13] which is the modified version of conventional finite element method (FEM) [14]. The idea of GraFEA is to reformulate the conventional FEM to make it suitable for modeling damage. GraFEA focuses on nodes and element edges (or links), rather than only elements. The magnitude of nodal forces is written in terms of axial strains along the element edges.

In diffuse approaches the fracture modeling assumes the sharp discontinuities in the material as a smeared damage. Continuum damage mechanics (CDM) is a continuous approach to model fracture [15] and dynamic fracture modeling using CDM is less studied [16–18]. Successful modeling of dynamic crack branching of concrete samples is presented using a nonlocal stress-based damage model in Ref. [19] and with a micropolar damage model regularized using the crack band method in Ref. [20]. Peridynamics [21] is a novel nonlocal CDM approach without spatial derivatives and can handle complex fracture behavior. An Eigen erosion approach to brittle fracture is proposed by [22]

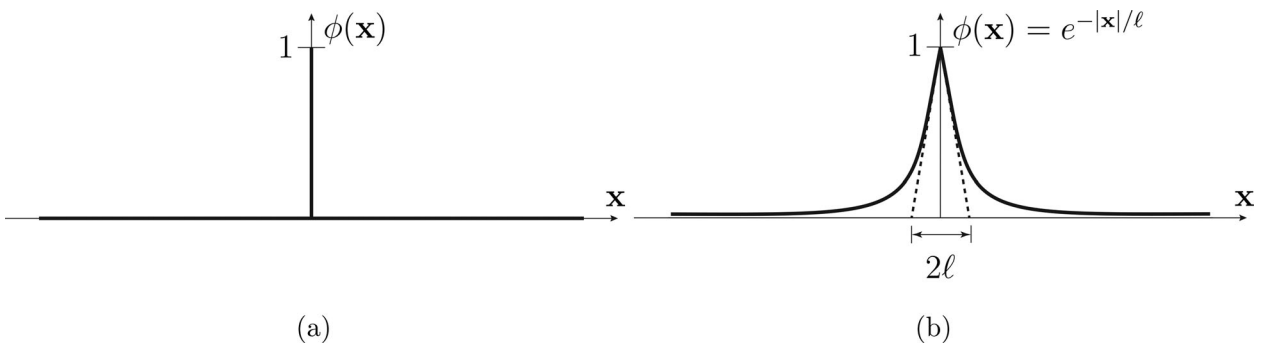


Figure 1. Crack topology. (a) Sharp (discrete) crack. (b) Smeared (diffuse) crack.

which is based on the general eigenfracture approach [23] by restricting the eigendeformations in a binary sense: they can be either zero (the local behavior is elastic) or they can be equal to the local displacement gradient (the material neighborhood is failed, or eroded).

The phase-field modeling is a diffuse approach [24, 25] based on variational formulation by energy minimization. This approach is more attractive as it can simulate complicated fracture processes, such as crack initiation, propagation, and branching. Propagation of cracks is automatically tracked by the evolution of the crack field which leads to a significant advantage over the discrete fracture methods, whose numerical implementation requires the handling of discontinuities. The derivation of the phase-field evolution equation and constitutive equation are based on the concepts of variational formulation by Francfort and Marigo [24], which extends the Griffith's theory of fracture and regularized by Bourdin et al. [26]. The quasi-static formulations have been extended to the dynamic case in Refs. [27–29].

In terms of implementation algorithms, the coupled system of phase-field models can be solved as either fully coupled fields (monolithic scheme) or sequentially coupled fields (staggered scheme) [30]. Li et al. [31] studied cell-based smoothed finite element method for predicting the crack propagation in solids. Borden et al. [28] account for high-order phase-field models [32] by incorporating it into the isogeometric analysis. The phase-field formulations can deal with cohesive fractures [33], multiphysics, large strain problems, and in ductile fracture.

The rate-dependence of micro-cracks evolution is not accounted in a phase-field evolution law equation. Kamensky et al. [34] worked on it by taking a micro-inertia contribution for phase-field evolution which are applied only for brittle fracture. To address this issue, Hai et al. [35] has incorporated the effect micro-inertia within the unified phase-field framework which accounts for damage evolution and are applied to quasi-brittle fracture.

In this work, we develop a phase-field model for dynamic brittle fracture based on the available literature using hybrid formulation and also by considering the micro-inertia effects. This model is applied for the quasi-static case by ignoring the inertia effects. A new way of implementation is done using Abaqus software to solve for the displacement field and the phase field. The staggered scheme is

implemented in user-defined subroutines to model both quasi-static and dynamic fracture. This implementation is different from implementations of [30, 31] in the way the user defined subroutines are developed. Here, the UMAT subroutine is used for solving the displacement field instead of using it just as a visualization layer. Several benchmark examples of dynamic and quasi-static fracture are solved to compare with existing numerical results.

The structure of the article is organized as follows. Section 2, presents the equations of the phase-field model which are based on the variational approach to brittle fracture. In Section 3, the implementation of the sequentially coupled phase-field model in Abaqus is presented. Several numerical examples under quasi-static and dynamic loading are investigated. Section 5, summarizes the whole article.

2. Formulation

2.1. Phase field approximation

Consider a bar of infinite length and cross section Γ aligned along x axis with a fully opened crack at $x = 0$. A Dirac delta function $\phi(x)$ is used to describe the sharp crack (see Figure 1(a)). Function $\phi(x)$ describes the crack phase-field with values zero in undamaged material and one for fully damaged. An exponential function is introduced to approximate the discrete crack topology by assuming the crack itself as a diffuse phenomenon and initiates with nano-voids and micro-cracks:

$$\phi(x) = e^{-|x|/\ell} \quad (1)$$

where $\phi(x)$ represents the diffuse crack topology and ℓ is the length scale parameter as shown in Figure 1(b).

Function $\phi(x)$ is the solution for the homogeneous differential equation:

$$\phi - \ell^2 \phi'' = 0 \quad \text{in } \Omega \quad (2)$$

with $\phi(0) = 1$ and at the limits $\phi(\pm\infty) = 0$.

Considering an elastic body Ω with internal crack surface Γ and surface boundary $\partial\Omega$, the crack surface is represented by a regularized crack surface function of the phase-field variable $\phi(x, t)$ (see Figure 2).

The total potential energy (Π) of the body in fracture modeling of materials is the sum of the crack surface energy and the deformation energy:

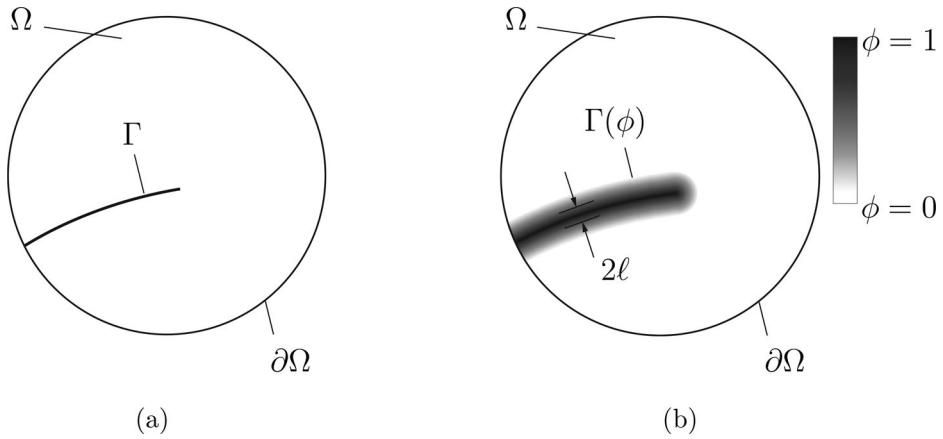


Figure 2. Body with internal crack. (a) Discrete crack. (b) Diffuse crack.

$$\Pi(\mathbf{u}, \Gamma) = \int_{\Omega} \Psi_e(\boldsymbol{\varepsilon}) dV + \int_{\Gamma} G_c d\Gamma \quad (3)$$

where Ψ_e is the elastic strain-energy density function, \mathbf{u} is the displacement, and G_c is the critical energy release rate.

The strain tensor can be defined in terms of displacement gradient by considering the small strain theory as follows:

$$\boldsymbol{\varepsilon} = \frac{1}{2} (\nabla \mathbf{u} + \nabla^T \mathbf{u}) \quad (4)$$

By using the variational principle of Eq. (2), the crack surface energy is approximated by

$$\int_{\Gamma} G_c d\Gamma \approx \int_{\Omega} G_c \left[\frac{\phi^2}{2\ell} + \frac{\ell}{2} |\nabla \phi|^2 \right] dV \quad (5)$$

where ℓ is the regularization parameter, which controls the width of the smooth approximation of the crack.

To consider the failure only due to tension and maintain failure in compression, the strain tensor is decomposed into positive and negative parts as follows:

$$\boldsymbol{\varepsilon}^{\pm} = \sum_{a=1}^n \langle \boldsymbol{\varepsilon}_a \rangle^{\pm} \mathbf{n}_a \otimes \mathbf{n}_a \quad (6)$$

where $\boldsymbol{\varepsilon}^+$ and $\boldsymbol{\varepsilon}^-$ represent the tensile and compressive modes of $\boldsymbol{\varepsilon}$, respectively. $\boldsymbol{\varepsilon}_a$ and \mathbf{n}_a are the eigenvalues and eigenvectors of $\boldsymbol{\varepsilon}$ in n dimensions. The Macaulay bracket has the meaning, $\langle x \rangle_{\pm} = (x \pm |x|)$. Therefore, the elastic energy can be decomposed into a positive part and a negative part [36]:

$$\psi_e^{\pm}(\boldsymbol{\varepsilon}) = \frac{\lambda}{2} \langle \text{tr}(\boldsymbol{\varepsilon}) \rangle^2 + \mu \text{tr}[(\boldsymbol{\varepsilon}^{\pm})^2] \quad (7)$$

where ψ_e^+ and ψ_e^- represent the tensile and compressive modes in ψ_e , respectively.

In hybrid formulation, the total strain energy is degraded as given below:

$$\int_{\Omega} \Psi_e(\boldsymbol{\varepsilon}) dV = \int_{\Omega} [(1 - \phi)^2 + k] \psi_e(\boldsymbol{\varepsilon}) \quad (8)$$

where $k \ll 1$ is a model parameter which prevents numerical singularity in the case of fully damaged system,

$$\psi_e(\boldsymbol{\varepsilon}) = \frac{1}{2} \boldsymbol{\sigma}_0 \boldsymbol{\varepsilon}$$

and $\boldsymbol{\sigma}_0$ is a elastic stress tensor.

2.2. Governing equations

For a dynamic problem, the kinetic energy of the body is given by

$$T(\dot{\mathbf{u}}) = \int_{\Omega} \frac{1}{2} \rho \dot{\mathbf{u}} \cdot \dot{\mathbf{u}} dV + \int_{\Omega} \frac{1}{2} \kappa \dot{\phi}^2 dV \quad (9)$$

where ρ is the mass density of the material, $\dot{\mathbf{u}}$ denotes the local velocity, and κ is a micro-mass density that quantifies the micro-inertia as the crack evolves.

The Lagrangian (L) is expressed as the difference between kinetic energy (T) and potential energy (Π):

$$L = T - \Pi = \int_{\Omega} \frac{1}{2} \rho \dot{\mathbf{u}} \cdot \dot{\mathbf{u}} dV + \int_{\Omega} \frac{1}{2} \kappa \dot{\phi}^2 dV - \int_{\Omega} [(1 - \phi)^2 + k] \psi_e(\boldsymbol{\varepsilon}) - \int_{\Omega} G_c \left[\frac{\phi^2}{2\ell} + \frac{\ell}{2} |\nabla \phi|^2 \right] dV \quad (10)$$

Using Hamilton's principle, the variation of the Lagrangian L with respect to the fields $\{\mathbf{u}, \phi\}$, considering $\delta \mathbf{u} = 0$ on $\partial\Omega$, yields following Euler–Lagrange equations in the domain Ω :

$$\nabla \cdot \boldsymbol{\sigma} = \rho \ddot{\mathbf{u}} \quad (11a)$$

$$\kappa \ddot{\phi} + \left(\frac{G_c}{\ell} + 2H \right) \phi - G_c \ell \Delta \phi = 2H \quad (11b)$$

with the boundary conditions

$$\boldsymbol{\sigma} \cdot \mathbf{n} = \mathbf{t} \text{ on } \partial\Omega_t \quad (12a)$$

$$\nabla \phi \cdot \mathbf{n} = 0 \text{ on } \partial\Omega \quad (12b)$$

The stress tensor is obtained as the derivative of the elastic strain energy with respect to the strain:

$$\boldsymbol{\sigma} = [(1 - \phi)^2 + k] C_0 \boldsymbol{\varepsilon} \quad (13)$$

where C_0 is the constitutive matrix.

The local history field H is taken as the maximum positive reference energy to ensure crack irreversibility to prevent cracks from healing when ψ_e^+ decreases,

$$H = \max_{s \in [0, t]} \psi_e^+(\boldsymbol{\varepsilon}(\mathbf{x}, s)) \quad (14)$$

A viscous regularization of the above formulation is formulated in terms of variational principle by including a modified extended dissipation functional in the potential as described in [36]. Equation (11b) may be recast into the viscous regularized format as follows:

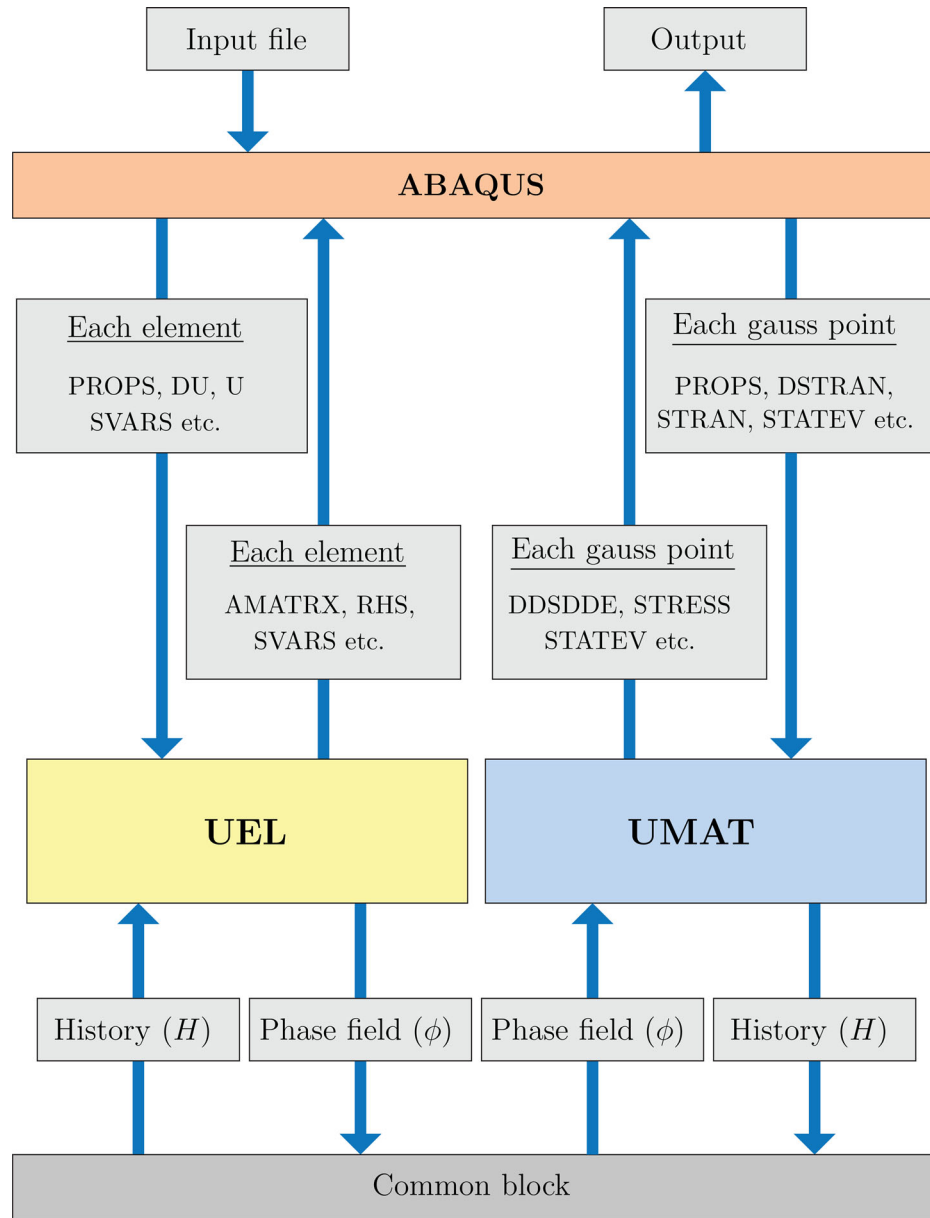


Figure 3. Flow chart showing the Abaqus implementation.

$$\kappa \ddot{\phi} + \left(\frac{G_c}{\ell} + 2\psi_e^+ \right) \phi - G_c \ell \Delta \phi + \eta \dot{\phi} = 2\psi_e^+ \quad (15)$$

where $\eta \geq 0$ is the viscous regularization parameter.

3. Numerical implementation

3.1. Weak forms of the governing equations

The weak forms of the Eqs. (11a) and (15) are formulated as follows:

$$\int_{\Omega} (-\rho \mathbf{u} \cdot \delta \mathbf{u} - \boldsymbol{\sigma} : \delta \boldsymbol{\epsilon}) dV + \int_{\Omega_r} \mathbf{t} \cdot \delta \mathbf{u} dA = 0 \quad (16a)$$

$$\begin{aligned} \int_{\Omega} -2(1-\phi)\delta\phi H dV + \int_{\Omega} \kappa \ddot{\phi} \delta\phi dV \\ + \int_{\Omega} G_c \left(\ell \nabla \phi \cdot \nabla \delta \phi + \frac{1}{\ell} \phi \delta \phi \right) dV + \int_{\Omega} \eta \dot{\phi} \delta \phi dV = 0 \end{aligned} \quad (16b)$$

The nodal values are approximated as follows:

$$\mathbf{u} = \sum_{i=1}^n N_i \mathbf{u}_i, \quad \phi = \sum_{i=1}^n N_i \phi_i \quad (17)$$

where n is the total number of nodes per element and N_i is the i th node shape function. The corresponding spacial derivative matrices and the gradients can be expressed as shown in Eqs. (18) and (19), respectively.

$$\mathbf{B}_i^u = \begin{bmatrix} N_{i,x} & 0 \\ 0 & N_{i,y} \\ N_{i,y} & N_{i,x} \end{bmatrix}, \quad \mathbf{B}_i^\phi = \begin{bmatrix} N_{i,x} \\ N_{i,y} \end{bmatrix} \quad (18)$$

$$\boldsymbol{\epsilon} = \sum_{i=1}^n \mathbf{B}_i^u \mathbf{u}_i, \quad \nabla \phi = \sum_{i=1}^n \mathbf{B}_i^\phi \phi_i \quad (19)$$

The element contribution at node i to the residual of the overall system of equations are formulated as follows:

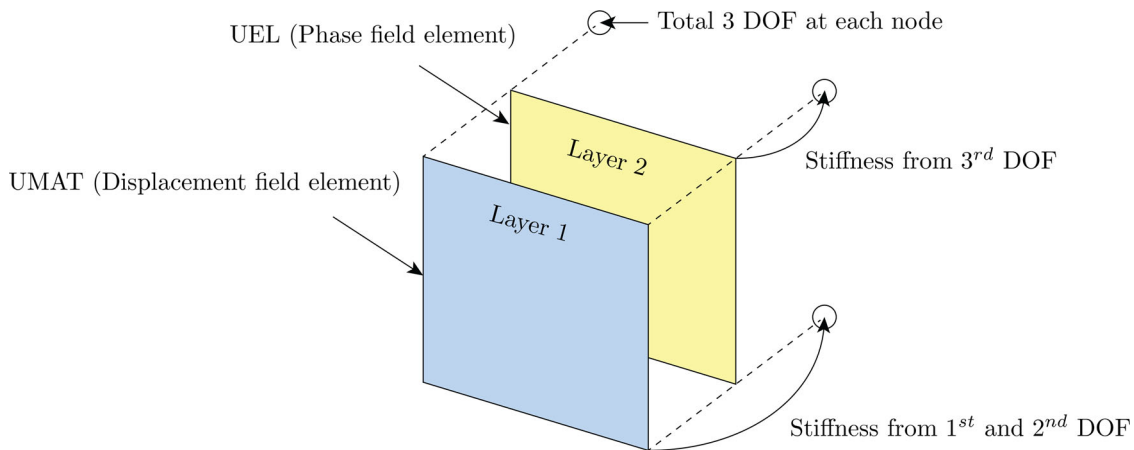


Figure 4. Two layered implementation in Abaqus.

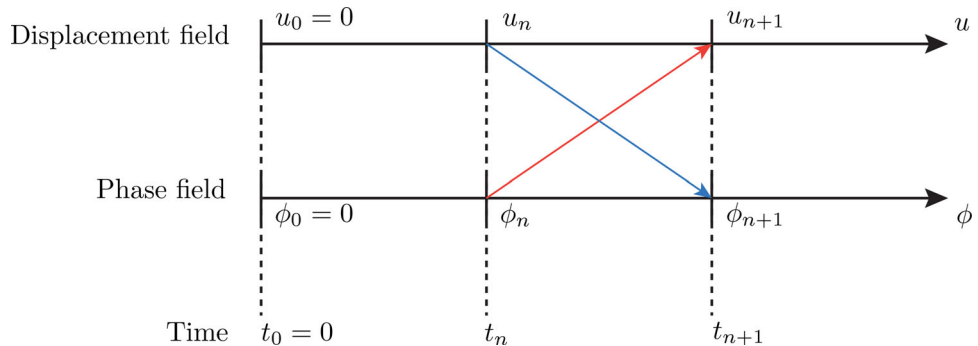


Figure 5. Staggered solution representation.

$$\mathbf{R}_i^u = \mathbf{F}_i^{u,\text{ext}} - \mathbf{F}_i^{u,\text{int}} - \mathbf{F}_i^{\text{ine}} \quad (20)$$

$$\mathbf{R}_i^\phi = -\mathbf{F}_i^{\phi,\text{int}} \quad (21)$$

where

$$\mathbf{F}_i^{u,\text{ext}} = \int_{\delta\Omega} N_i \mathbf{f} dA \quad \text{and} \quad \mathbf{F}_i^{u,\text{int}} = \int_{\Omega} \mathbf{B}_i^u \boldsymbol{\sigma} dV$$

are the external force and internal force, respectively, corresponding to displacement.

$$\mathbf{F}_i^{\text{ine}} = \int_{\Omega} \rho N_i \mathbf{u} .. dV$$

is the force of inertia.

$$\mathbf{F}_i^{\phi,\text{int}} = - \int_{\Omega} \left(2(1-\phi)N_i H - \kappa \ddot{\phi} N_i - G_c \left(\ell [\mathbf{B}_i^\phi]^T \nabla \phi + \frac{1}{\ell} N_i \dot{\phi} \right) - \eta \dot{\phi} N_i \right) dV$$

is the internal force corresponding to phase field.

The element level tangent matrices are obtained from the internal forces as follows:

$$\mathbf{K}_{ij}^{uu} = \frac{\partial \mathbf{F}_i^{u,\text{int}}}{\partial \mathbf{u}_j} = \int_{\Omega} [(1-\phi)^2 + k] [\mathbf{B}_i^u]^T C_0 [\mathbf{B}_j^u] dV \quad (22)$$

$$\begin{aligned} \mathbf{K}_{ij}^{\phi\phi} &= \frac{\partial \mathbf{F}_i^{\phi,\text{int}}}{\partial \phi_j} \\ &= \int_{\Omega} \left([\mathbf{B}_i^\phi]^T G_c \ell [\mathbf{B}_j^\phi] + N_i \frac{\kappa}{\Delta t^2} N_j + N_i \left(2H + \frac{G_c}{\ell} \right) N_j + N_i \frac{\eta}{\Delta t} N_j \right) dV \end{aligned} \quad (23)$$

3.2. Abaqus implementation

The nonlinear system of equations require iterative schemes for calculating the solution. Abaqus software is used for the implementation to take the advantage of its built-in nonlinear solver which employs the Newton–Raphson algorithm. A four-node quadrilateral element with 3 degrees of freedom at each node (u_1 , u_2 , and ϕ) under plane strain condition is chosen for the analysis. Abaqus implementation is carried out using UMAT and UEL subroutines, as shown in Figure 3.

Two layers for each element are created to do the calculations in each layer separately as shown in Figure 4. UMAT subroutine is used for one layer to calculate the displacements u_1 , u_2 , and UEL subroutine on the other layer for the calculation of ϕ .

Abaqus UEL subroutine allows for the user defined calculations of the element stiffness matrix and the residual force vector. The ϕ value calculated in UEL subroutine is passed to the UMAT subroutine using a common block variable. This common block variable also passes the energy calculated in UMAT subroutine to UEL subroutine. The ϕ values passed to the UMAT layer are used for the calculation of degradation function and the energy values passed to UEL layer are used for calculating the corresponding history energy values responsible for the crack evolution. The ϕ values at each integration point are stored as the state variable in an array called STATEV available in UMAT subroutine

which allows for contour plot of crack profile ϕ . The displacement and phase fields of this coupled system is solved as a sequentially coupled fields using the staggered method. In a staggered scheme two fields are solved independently in every load step. The phase field for the displacement field element and the history energy for the phase field element are updated only in the first iteration of each load step. The iteration process for the present staggered scheme is shown in Figure 5 and it is slightly different from the staggered scheme proposed by [36].

Algorithm 1: Staggered scheme for phase field fracture

1. *Initialization:* Displacement (u_n), phase field (ϕ_n), and history (H_n) are known at time t_n
2. *Apply loads:* Update prescribed loads \bar{u}, \bar{t} at current time t_{n+1} with $\Delta t = t_{n+1} - t_n$
3. *Compute history:*

$$H_{n+1} = \begin{cases} \psi_{0,n}^+(\boldsymbol{\varepsilon}) & \text{for } \psi_{0,n}^+(\boldsymbol{\varepsilon}) > H_n \\ H_n & \text{otherwise} \end{cases}$$

4. *Compute phase field:*

$$\phi_{n+1} = \operatorname{Arg} \inf_{\phi} \left\{ \int_{\Omega} \left[\frac{1}{2} \kappa \left(\frac{\phi - \phi_n}{\Delta t} \right)^2 - [(1-\phi)^2 + k] H_{n+1} - G_c \gamma \right] dV \right\}$$

where

$$\gamma = \left[\frac{\phi^2}{2\ell} + \frac{\ell}{2} |\nabla \phi|^2 \right]$$

5. *Compute displacement field:*

$$\begin{aligned} u_{n+1} = \operatorname{Arg} \inf_{\boldsymbol{u}} \left\{ \int_{\Omega} \left[\rho \frac{4}{(\Delta t)^2} \left(\frac{1}{2} |\boldsymbol{u}|^2 - \tilde{\boldsymbol{u}}_n \cdot \boldsymbol{u} \right) \right. \right. \\ \left. \left. + [(1-\phi_n)^2 + k] \psi_{0,n+1}(\boldsymbol{\varepsilon}) \right] dV - \int_{\Omega_T} \boldsymbol{t} \cdot \boldsymbol{u} dA \right\} \end{aligned}$$

where

$$\tilde{\boldsymbol{u}}_n = \boldsymbol{u}_n + \dot{\boldsymbol{u}}_n \Delta t + \frac{1}{4} \ddot{\boldsymbol{u}}_n \Delta t^2$$

6. *Store variables:* Store Displacement (u_{n+1}), phase field (ϕ_{n+1}) and history (H_{n+1}) as history variables.

4. Numerical examples

The performance of the present phase field model is investigated for various quasi-static and dynamic benchmark examples using implicit analysis.

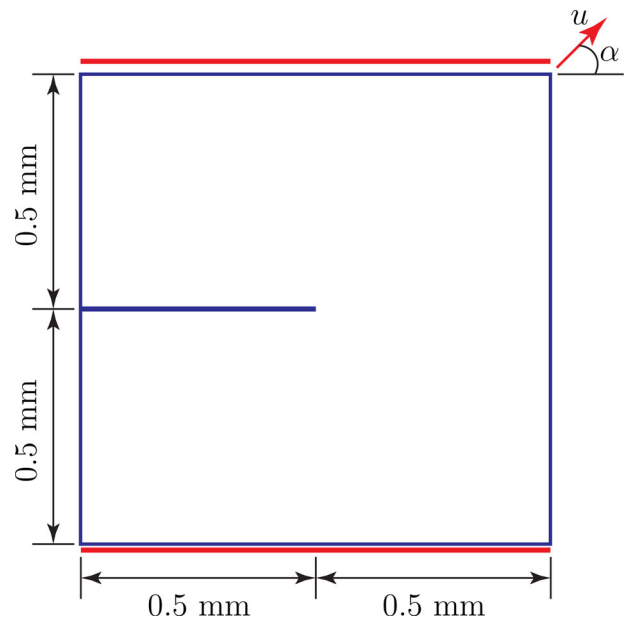


Figure 6. Geometry and boundary conditions for single edge notched specimen.

4.1. Single edge notched specimen

A single horizontal edge notch square plate is considered as the first example. The geometry and loading conditions are as shown in Figure 6. Displacement load is applied at the top of the specimen whose direction is specified by α . When $\alpha = 90^\circ$ the loading is pure tension and when $\alpha = 0^\circ$ the loading is pure shear. The mesh is refined only in the regions where the crack is expected to occur and propagate to reduce the computational cost. The material parameters chosen for the analysis are Young's modulus $E = 210$ GPa, Poisson's ratio $\nu = 0.3$ and the critical energy release rate to $G_c = 2700$ J/m²

4.1.1. Single edge notched tension test

To compare the present results with the literature [36] simulations are performed for two different length scale parameters $\ell = 0.0150$ mm and 0.0075 mm for a mesh size of $h = 0.0010$ mm. The crack patterns for two length scales are shown in Figure 7 and it is observed that crack width reduces with the length scale parameter. Figure 8 shows the reaction force for different length scale parameters ℓ compared with the results by Miehe et al. [36]. It is seen that the peak load is in agreement and there is a small deviation in the propagation period. To study the effect which arises due to the mesh size different simulations are performed for $h = 0.0055$ mm, 0.0035 mm, and 0.0010 mm. The crack patterns and load-displacement curves are shown in Figures 9 and 10, respectively. It can be observed that the peak load is decreasing as the mesh is becoming finer.

4.1.2. Single edge notched shear test

To study the effect of length scale parameter, simulations are performed for two different length scale parameters $\ell = 0.0150$ mm and 0.0075 mm for a mesh size of

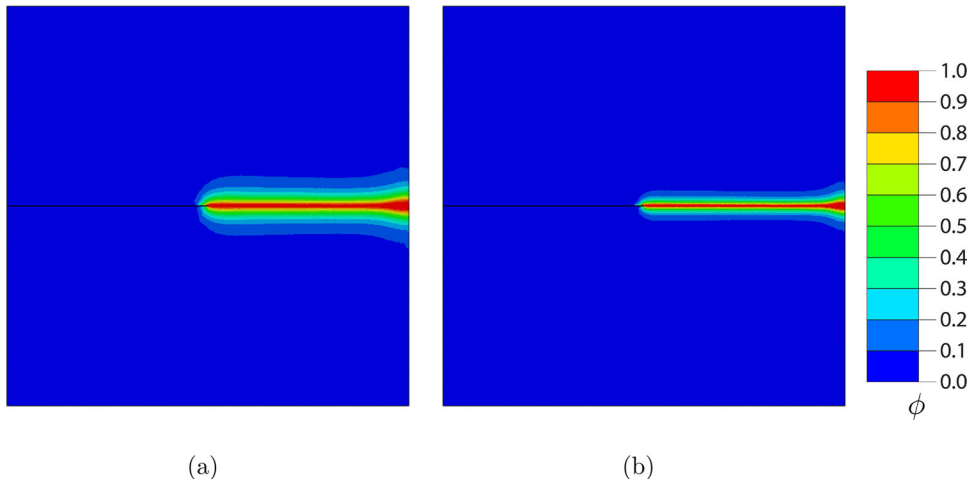


Figure 7. Crack patterns for single edge notched tension test for two length scales with mesh size $h = 0.0010$ mm. (a) $\ell = 0.0150$ mm. (b) $\ell = 0.0075$ mm.

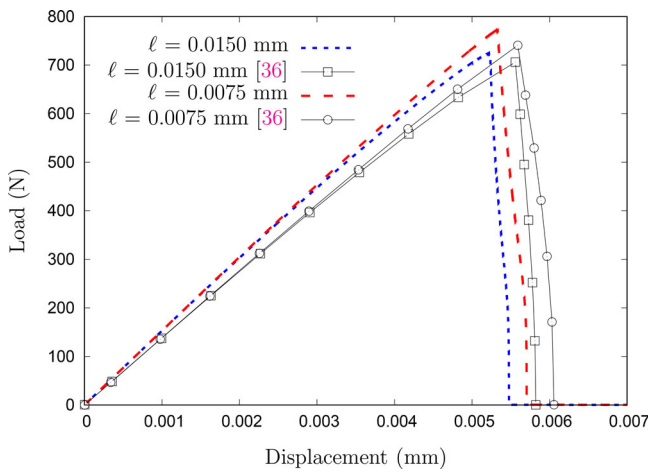


Figure 8. Load-Displacement curve for single edge notched tension test for two length scales.

$h = 0.0035$ mm. Figure 11 crack pattern for two length scales and the profiles are similar to the crack patterns given by [36] and load versus displacement curves are shown in and Figure 12 and it can be observed that the peak load increases with the decrease in length scale parameter.

4.2. Symmetric three point bending test

To test the model in a bending problem a three point bending test is considered. The geometric setup and the boundary conditions are illustrated in Figure 13. The material properties used are $E = 20.8$ GPa and $\nu = 0.3$, $G_c = 500$ J/m 2 , $\ell = 0.03$ mm, and $h = 0.01$ mm. To study the effect which arise due to the critical energy release rate different simulations are performed for $G_c = 500$ J/m 2 , 600 J/m 2 , and 700 J/m 2 . Figure 14 shows the crack initiation and propagation. The crack initiates at the displacement of 0.049 mm and propagates after that till maximum applied displacement of 0.1 mm. The load-displacement curves are shown in and

Figure 15, respectively, for different values of G_c . It is observed that the initiation of crack is delayed as the G_c value is increasing.

4.3. Asymmetric double notched tensile specimen

The geometry and loading conditions for asymmetric double notched specimen are illustrated in Figure 16. The following material properties are used: $E = 210$ GPa, $\nu = 0.3$, $G_c = 2700$ J/m 2 , and $\ell = 0.2$ mm. The mesh is well refined with the mesh size $h = 0.1$ mm in the expected crack region. The crack patterns and load-displacement curves are shown in Figures 17 and 18, respectively. The displacement increment plays an important role in predicting the post peak behavior. The smaller value of displacement increment gives more accurate result as the material stiffness is getting degraded more number of times for a given applied displacement after the post-peak. This will make the load to fall sharply after the post-peak (see Figure 18). For this example, the displacement increment has the effect on crack patterns (see Figure 17). The smaller displacement increment predicted the actual crack pattern and there is no complete separation of the material. In case of larger displacement increment, the two cracks have changed their paths and merged at the center once the crack tips have come closer to each other in their actual paths. There is a complete separation of the material when the larger displacement increment is used and hence the load falls to zero (see Figure 18).

4.4. Dynamic crack branching example

The geometry and boundary conditions are shown in Figure 19. To capture dynamic crack branching using the present model, a pre-notched brittle plate is modeled with an impact stress σ for three cases. Case 1: $\sigma = 1$ MPa, Case 2: $\sigma = 2.5$ MPa, and Case 3: Load profile shown in Figure 20. The material properties considered are $\rho = 2450$ kg/m 3 , $E = 32$ GPa, $\nu = 0.2$, and $G_c = 3$ J/m 2 . The model is meshed

with 0.25 mm element size and the length scale parameter considered is 0.5 mm. For Case 1, simulations are done for three different time step sizes $0.1 \mu\text{s}$, $0.05 \mu\text{s}$, and $0.025 \mu\text{s}$.

Case 1: Figure 21 shows the crack patterns for all the step sizes. Figure 22 shows the elastic strain energy curves

for all the step sizes. The elastic strain energy decreases as the time increases. The elastic strain energy is higher for larger time step and lower for smaller time step. Figure 23 presents the dissipation energy curves for the dynamic crack branching example. The dissipated energy increases with

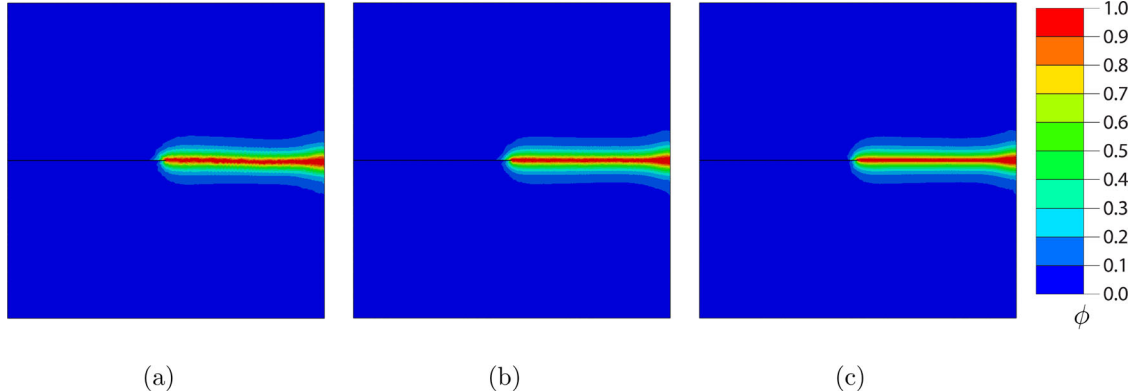


Figure 9. Crack patterns for single edge notched tension test for three mesh sizes at a length scale $\ell = 0.0150 \text{ mm}$. (a) $h = 0.0055 \text{ mm}$. (b) $h = 0.0035 \text{ mm}$. (c) $h = 0.0010 \text{ mm}$.

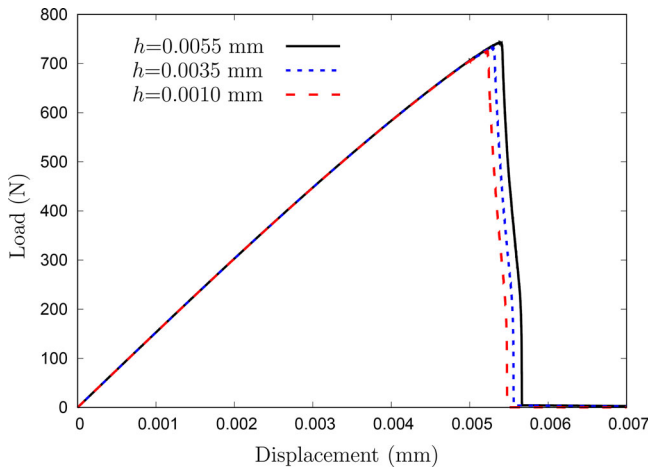


Figure 10. Load-Displacement curve for single edge notched tension test for three mesh sizes.

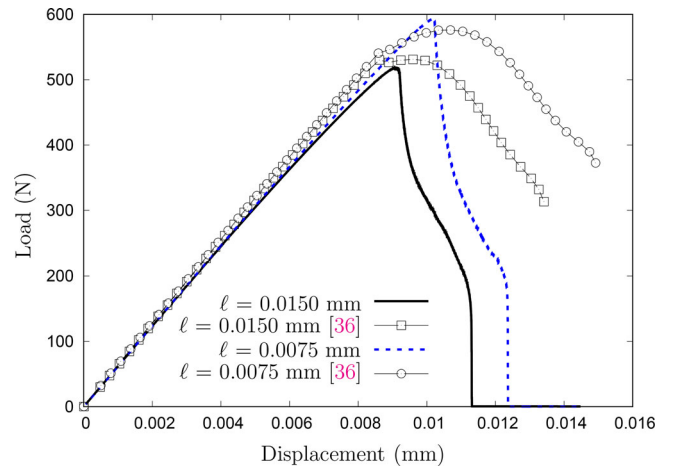


Figure 12. Load-Displacement curve for single edge notched tension test for two length scales.

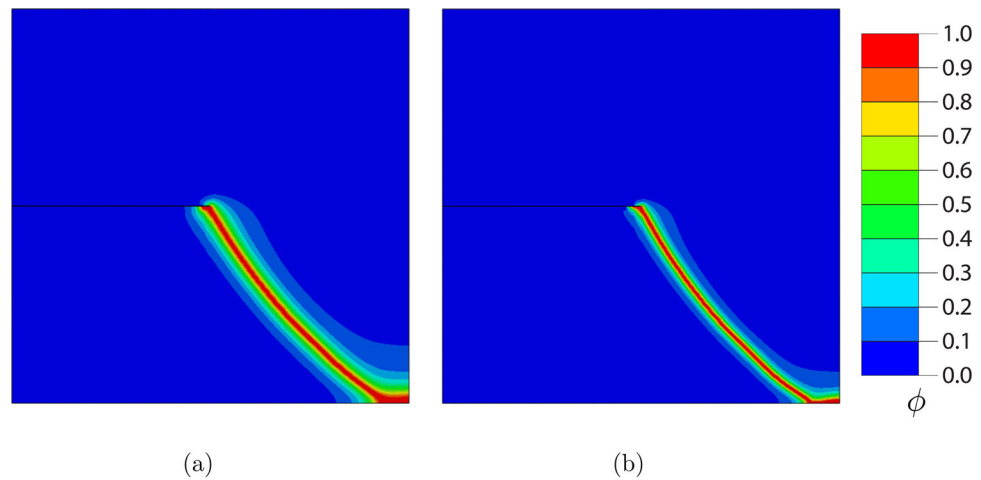


Figure 11. Crack patterns for single edge notched tension test for two length scales with mesh size $h = 0.0035 \text{ mm}$. (a) $\ell = 0.0150 \text{ mm}$. (b) $\ell = 0.0075 \text{ mm}$.

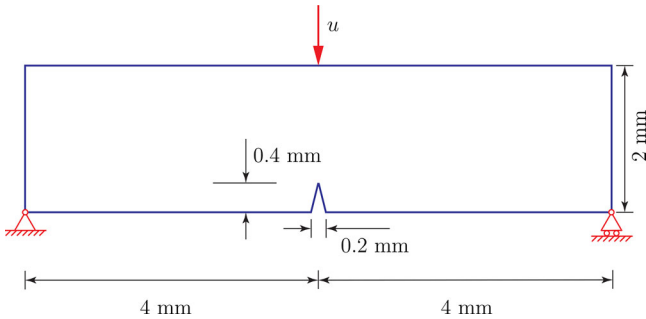


Figure 13. Geometry and boundary conditions for symmetric three point bending test.

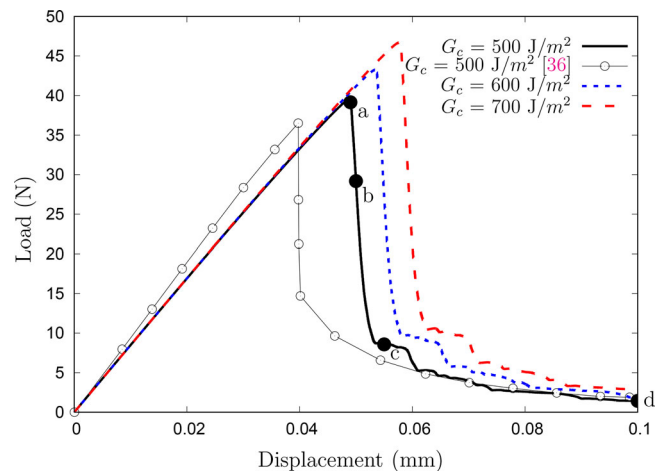


Figure 15. Load-Displacement curve for three point bending test for different G_c values.

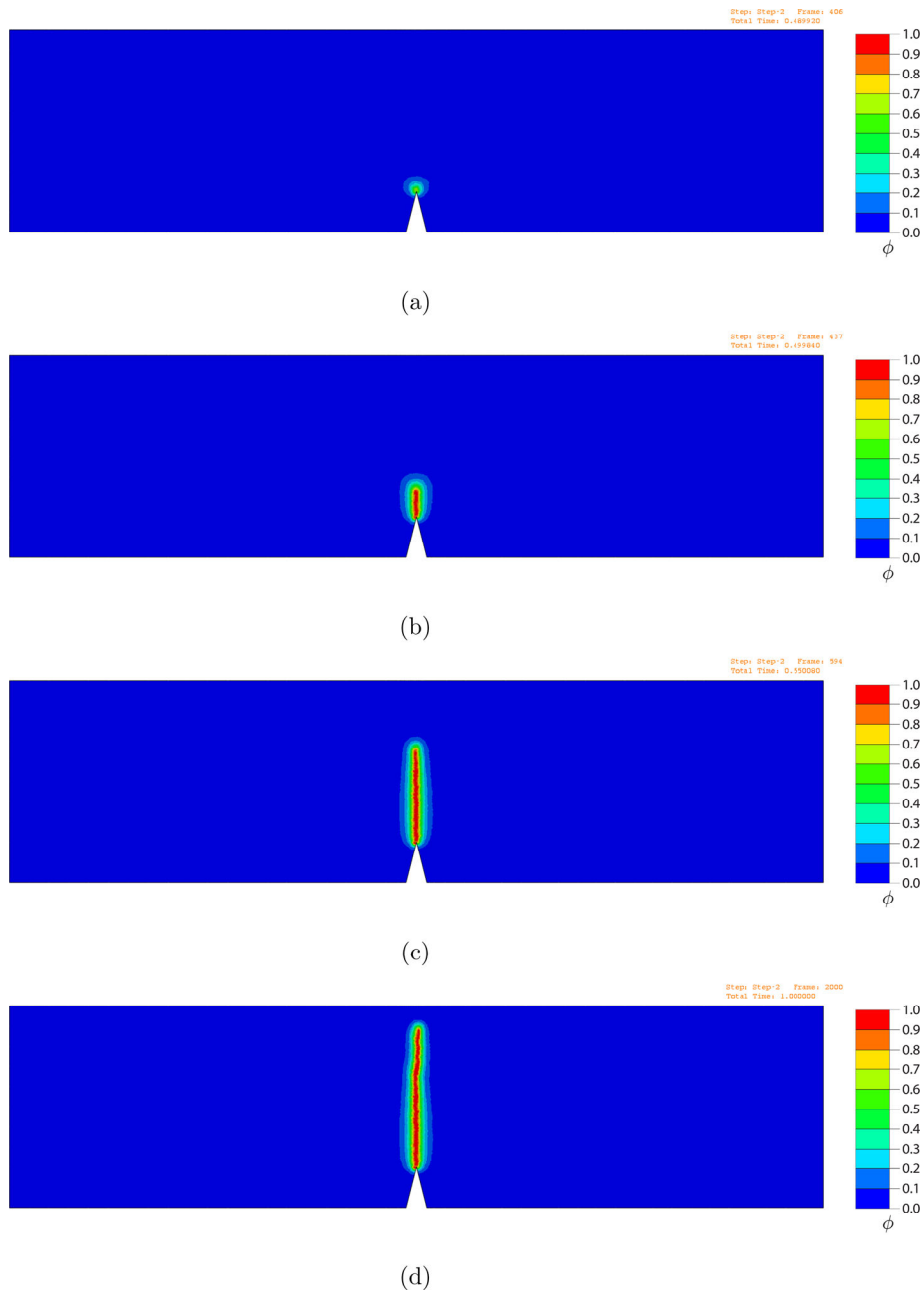


Figure 14. Damage profile for symmetric three point bending test. (a) $u = 0.049$ mm. (b) $u = 0.050$ mm. (c) $u = 0.055$ mm. (d) $u = 0.1$ mm.

time for all the time step sizes. The energy dissipation due to crack propagation is higher for smaller time step and lower for larger time step. From the energy curves, it can be inferred that the crack surface area formed for larger time step is more than the crack surface formed for smaller time step. The time increment size has little effect on the extent of crack propagation. For smaller time increments, the extent of crack is little larger compared to the extent of the crack for larger time increments. Also, the position of the crack branching got shifted toward the right (see Figure 21). After the crack initiation, as the extent of crack is depending on the time step size, more dissipation of energy is occurring for the smaller time increments. So the stored elastic strain energy for the smaller time increment is low (see Figure 22).

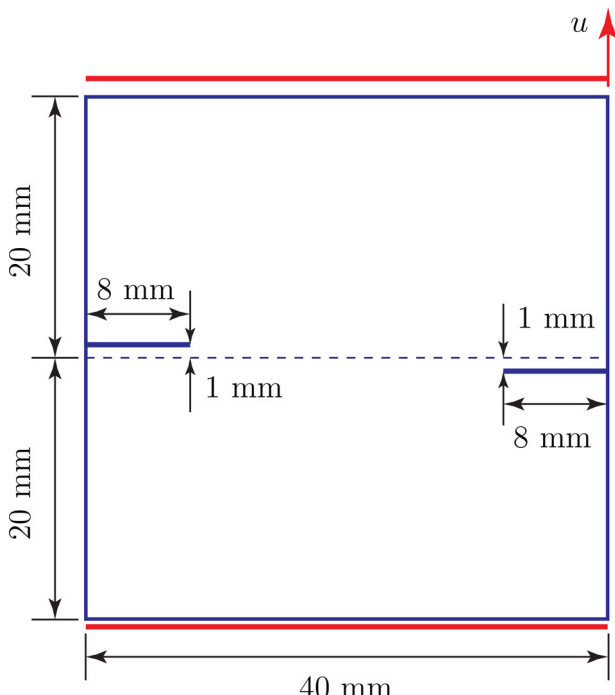


Figure 16. Geometry and boundary conditions for asymmetric double notched tensile specimen.

Case 2: Figure 24 shows the crack patterns and the multiple branching can be observed as the impact stress is increased in this case. The energy curves are shown in Figure 25.

Case 3: Figure 26 shows the crack patterns and the multiple branching can be observed in this case also. The energy curves are shown in Figure 27.

4.5. Kalthoff experiment

The second example considered for testing our model for dynamic fracture is the Kalthoff experiment where a double pre-notched steel plate is impacted by a projectile. The geometry and the boundary conditions are shown in Figure 28. To reduce the computational cost only half of the original geometry is modeled by imposing symmetry boundary condition. The projectile is impacted by an initial velocity v_0 which increases linearly with time to $t_0 = 1 \mu\text{s}$, and then, holds at $v_0 = 16.5 \text{ m/s}$. The material properties are $\rho = 8000 \text{ kg/m}^3$, $E = 190 \text{ GPa}$, $\nu = 0.3$, $G_c = 22.13 \text{ kJ/m}^2$, and $\kappa = 1.0e^{-8} \text{ kg/m}$. The length scale parameter is set to 0.39 mm, element size is taken as 0.195 mm. The simulations are done for three different velocities 16.5 m/s, 30 m/s, and

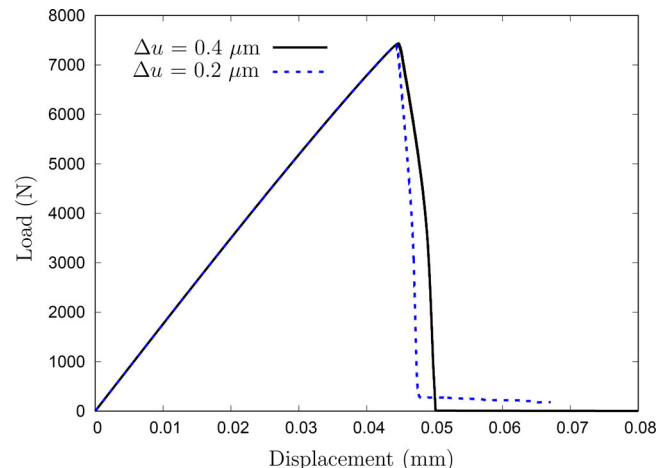


Figure 18. Load-Displacement curve for asymmetric double notched tensile specimen.

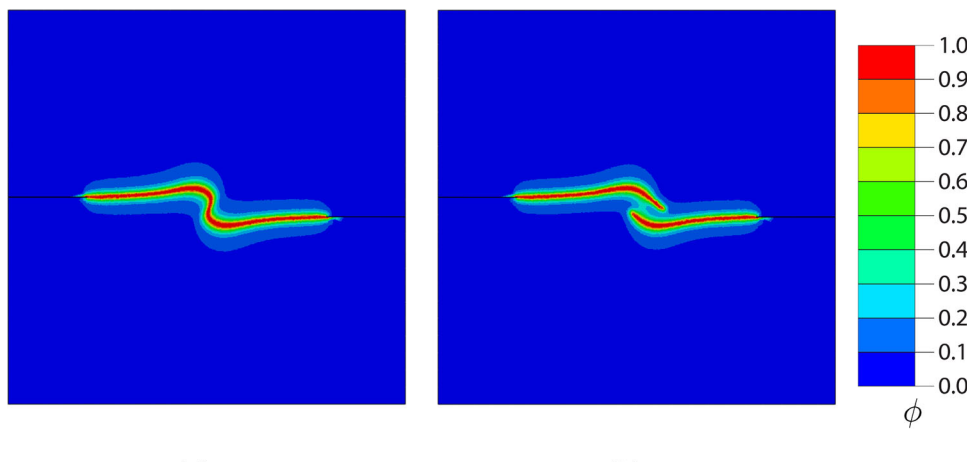


Figure 17. Damage profiles for asymmetric double notched tensile specimen. (a) $\Delta u = 0.4 \mu\text{m}$. (b) $\Delta u = 0.2 \mu\text{m}$.

50 m/s. Figure 29 shows crack patterns for three different velocities at 90 μ s. Figure 30 shows the elastic strain energy curves for three velocities. The maximum energy storage capacity is higher for higher rate of loading and it decreases with the decrease in loading rate. Figure 31 presents the dissipation energy curves for the Kalthoff experiment. The dissipation energy increases as the time increases for all the velocities considered. The energy dissipated for higher rate of loading is more than the lower rates of loading. From the

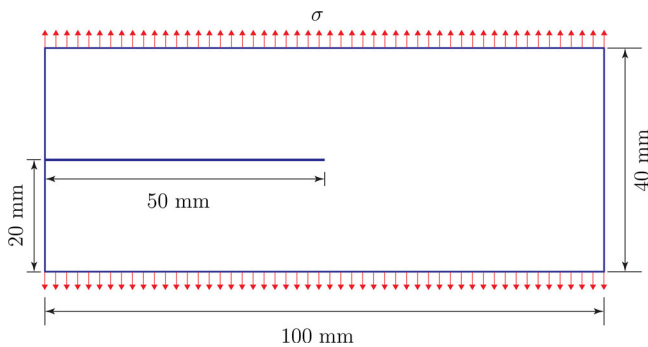


Figure 19. Geometry and boundary conditions for dynamic crack branching example.

energy curves it can be inferred that the crack surface area formed for higher rate of loading is more than the lower rates of loading.

4.6. Compact tension test in concrete

To test the phase field model for dynamic fracture, compact tension tests are performed on concrete [35]. The geometry and the boundary conditions are shown in Figure 32. The velocity v_0 is applied on the right edge of the notch while the left edge is fixed.

The material properties are $\rho = 2400 \text{ kg/m}^3$, $E = 36 \text{ GPa}$, $\nu = 0.18$, $G_c = 65 \text{ J/m}^2$, and $\kappa = 3.0e^{-9} \text{ kg/m}$. The length scale parameter is set to 1 mm, element size is taken as 0.5 mm. The simulations are done for three different velocities 0.304 m/s, 1.375 m/s, and 3.3 m/s. The velocity condition given in [35] is imposed while applying the velocity boundary condition (the velocity is increased from zero to v_0 until $t_0 = 100 \mu\text{s}$, and then, kept constant till the end of simulation).

The crack patterns obtained from the simulations and the crack patterns from the experiments shown in [20] are represented in Figure 33. The crack propagation and branching

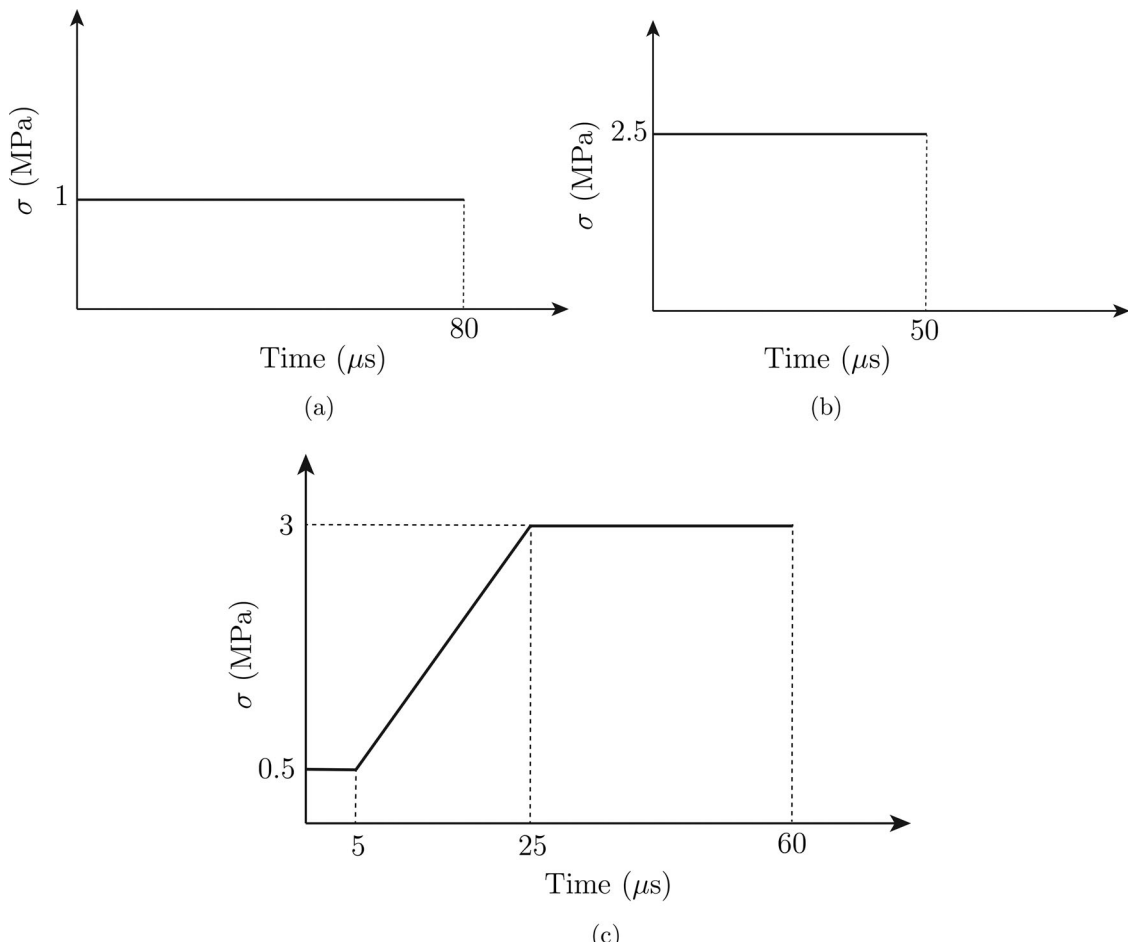


Figure 20. Load profiles for dynamic crack branching example. (a) Case 1. (b) Case 2. (c) Case 3.

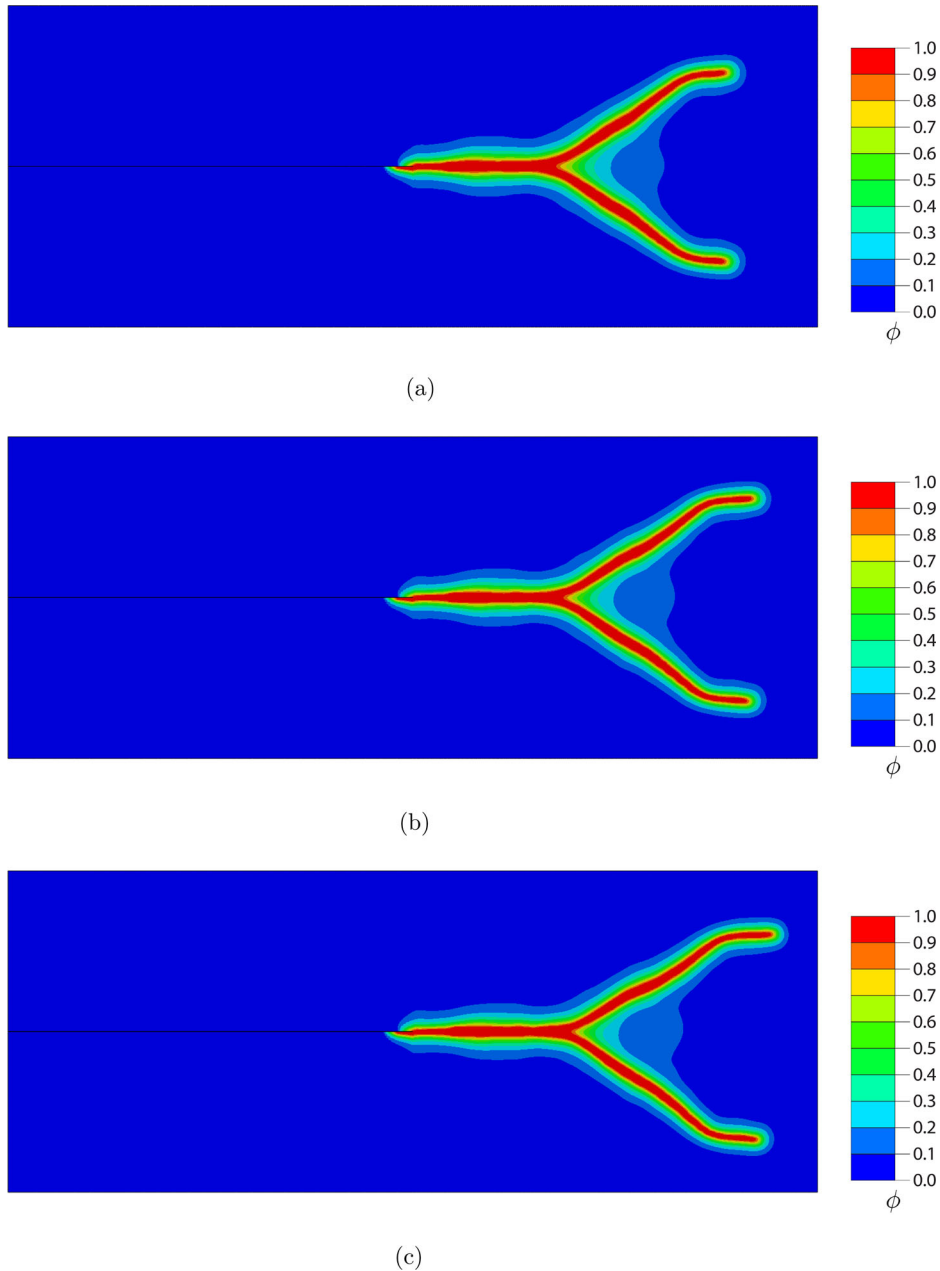


Figure 21. Damage profile for dynamic crack branching example for Case 1. (a) $\Delta t = 0.1 \mu s$. (b) $\Delta t = 0.05 \mu s$. (c) $\Delta t = 0.025 \mu s$.

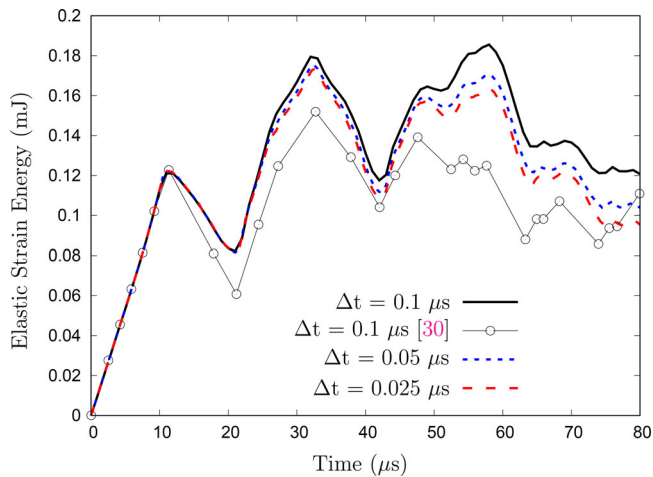


Figure 22. Strain energy curves for dynamic crack branching example for Case 1.

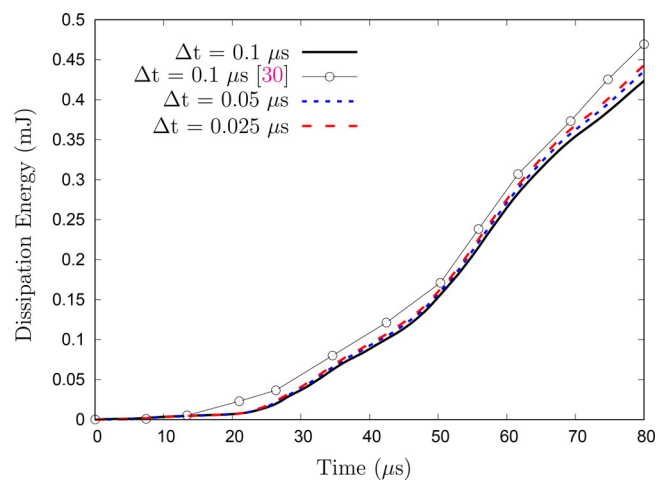


Figure 23. Dissipation energy curves for dynamic crack branching example for Case 1.

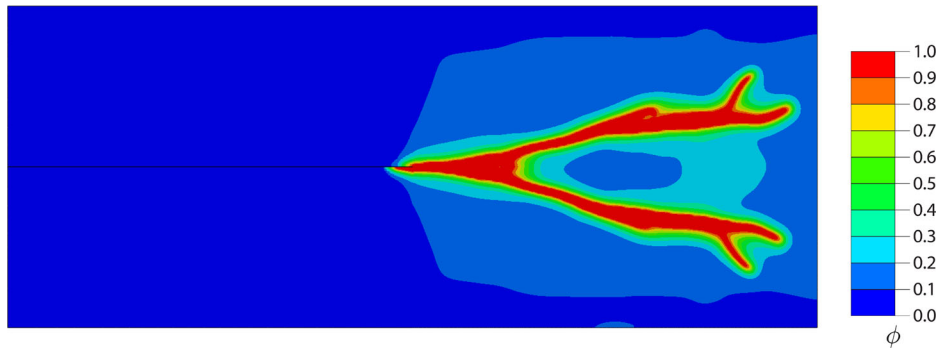


Figure 24. Damage profile for dynamic crack branching example for Case 2.

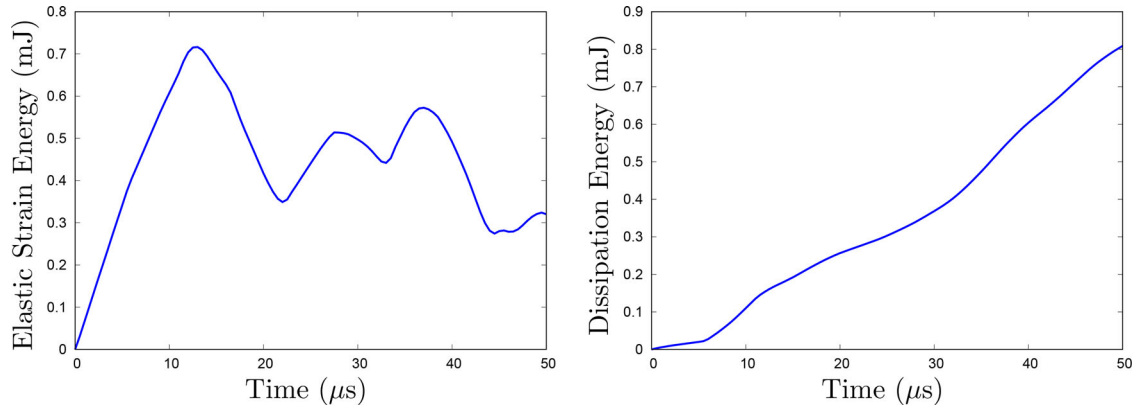


Figure 25. Energy curves for dynamic crack branching example for Case 2.

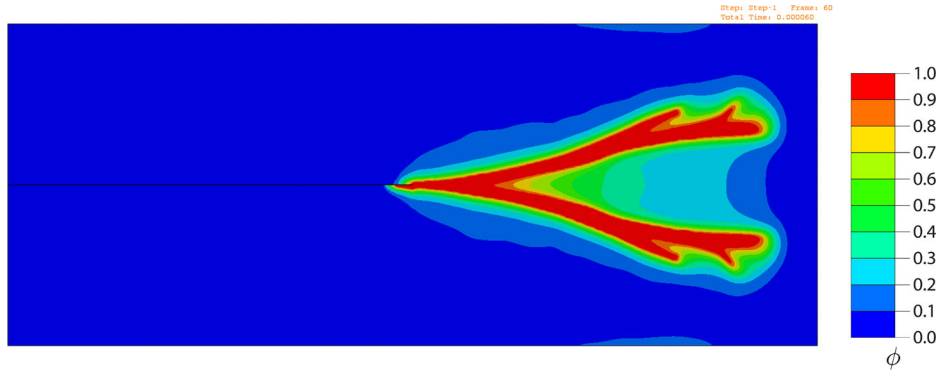


Figure 26. Damage profile for dynamic crack branching example for Case 3.

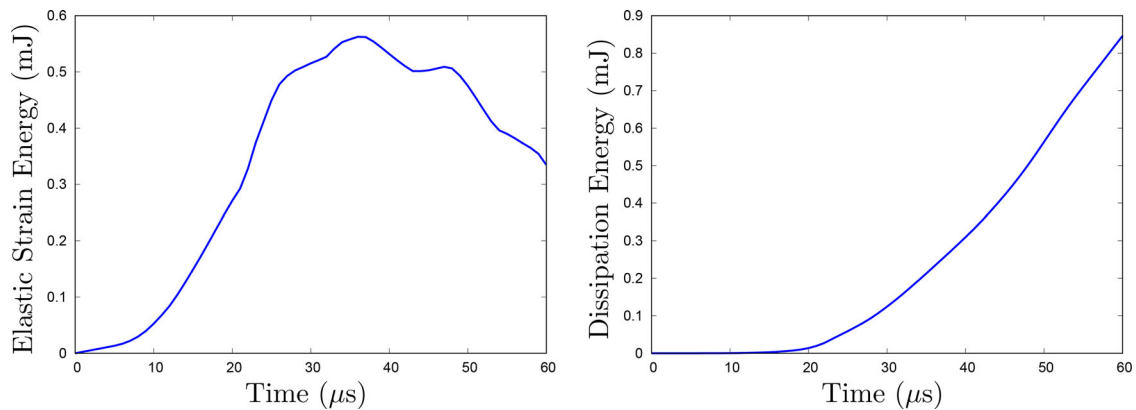


Figure 27. Energy curves for dynamic crack branching example for Case 3.

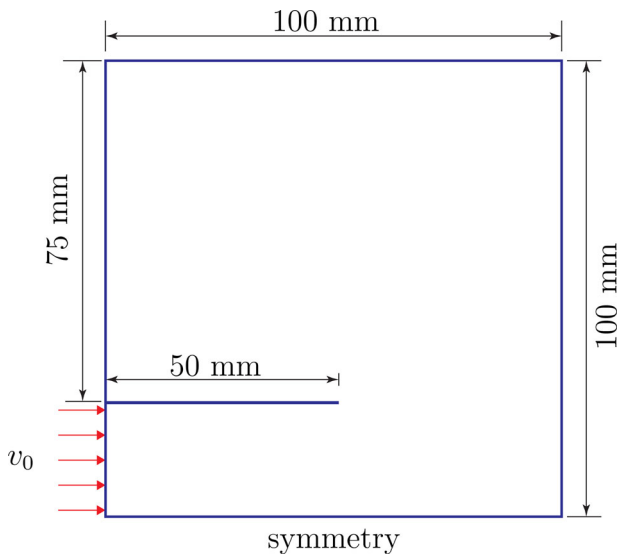


Figure 28. Geometry and boundary conditions for Kalthoff experiment.

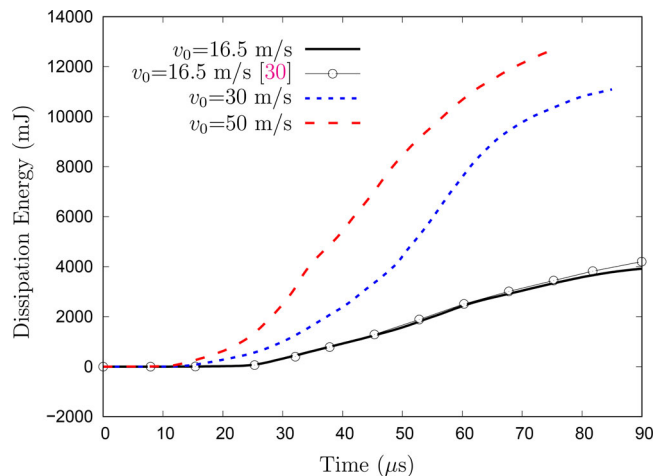


Figure 31. Dissipation energy curves for Kalthoff experiment.

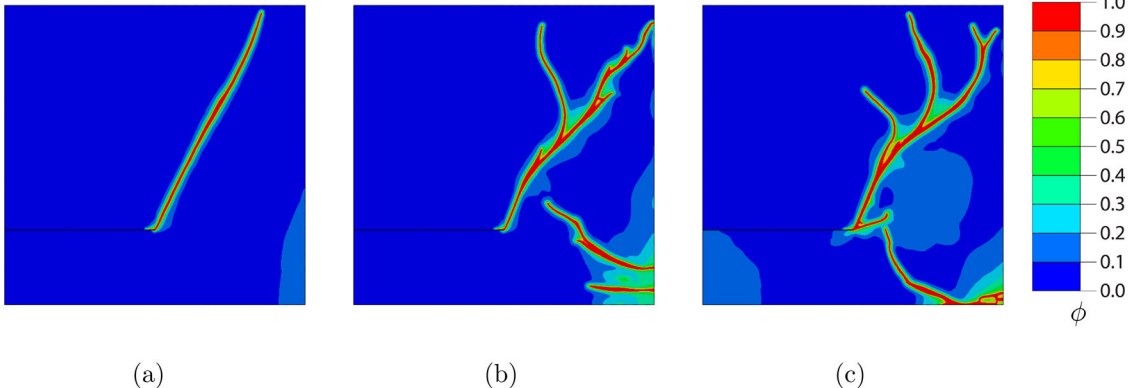


Figure 29. Damage profile for Kalthoff experiment. (a) $v_0=16.5$ m/s. (b) $v_0=30$ m/s. (c) $v_0=50$ m/s.

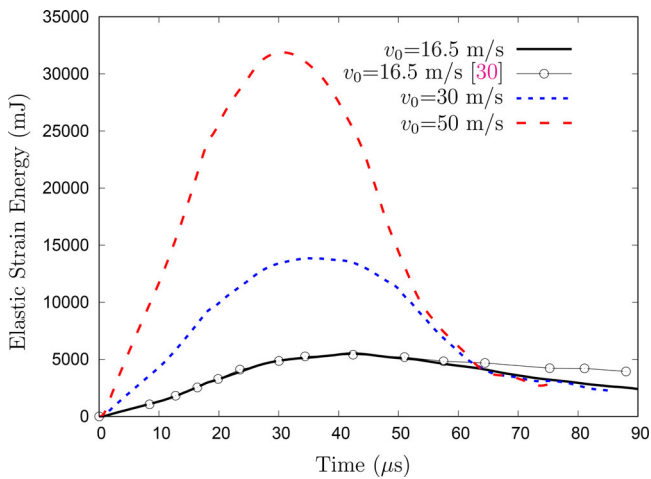


Figure 30. Strain energy curves for Kalthoff experiment.

are in good agreement with the experimental results. The elastic strain energy curves for three different velocities are shown in Figure 34. The maximum energy storage capacity is higher for higher rate of loading and it decreases with the decrease in loading rate. Figure 35 presents the dissipation energy curves. The dissipation energy increases as the time

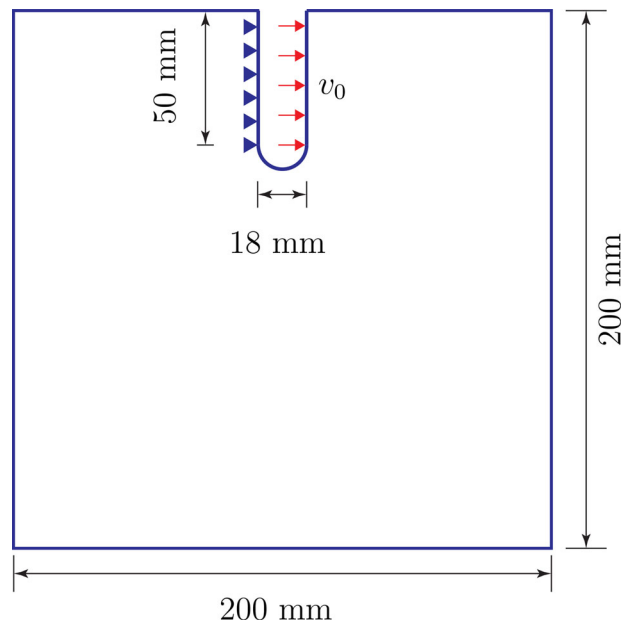


Figure 32. Geometry and boundary conditions for compact tension test.

increases for all the velocities considered. The energy dissipated for higher rate of loading is more than the lower rates of loading. From the energy curves, it can be inferred that

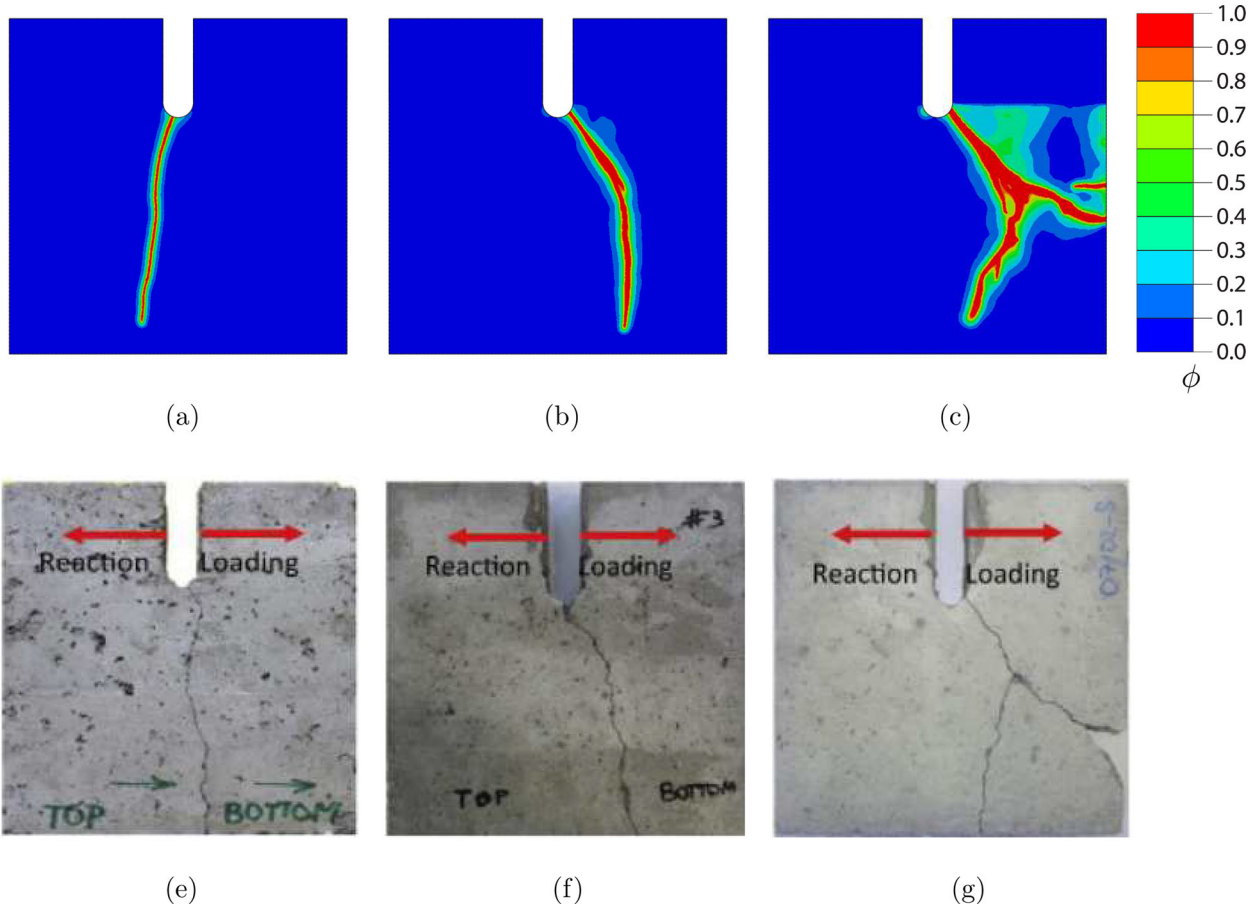


Figure 33. Damage profile for compact tension tests in Concrete. (a) $v_0 = 0.304 \text{ m/s}$. (b) $v_0 = 1.375 \text{ m/s}$. (c) $v_0 = 3.3 \text{ m/s}$. (d). (e) $v_0 = 0.304 \text{ m/s}$. (f) $v_0 = 1.375 \text{ m/s}$. (g) $v_0 = 3.3 \text{ m/s}$.

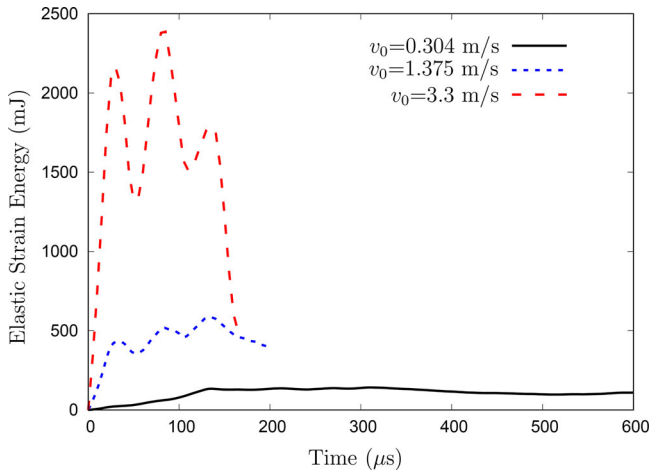


Figure 34. Strain energy curves for compact tension tests in Concrete.

the crack surface area formed for higher rate of loading is more than the lower rates of loading.

5. Conclusions

In this article, a new procedure for Abaqus implementation is presented in solving the two equilibrium equations of the phase field model. The implementation is carried out for the two-dimensional problem based on the Abaqus user subroutines UMAT and UEL. The difference in the implementation is in

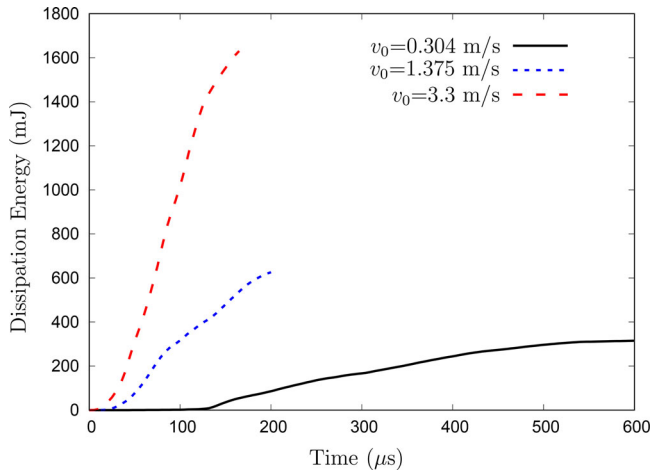


Figure 35. Dissipation energy curves for compact tension tests in Concrete.

the development of UMAT subroutine that is used for finding the displacement field. The UEL subroutine is used only for finding the crack phase field unlike the way it is used in other literature. The present procedure of Abaqus implementation will reduce some computational time. The utility of the method is understood through several quasi-static and dynamic examples. The effect of size of the finite elements is very less on the force response when the mesh size is smaller than the half of the length scale parameter (ℓ). The correct choice of load step is very important for achieving accurate results.

ORCID

Junuthula N. Reddy  <http://orcid.org/0000-0002-9739-1639>

References

- [1] A.A. Griffith, The phenomena of rupture and flow in solids, *Philos. Trans. R. Soc. A: Math. Phys. Eng. Sci.*, vol. 221, no. 582–593, pp. 163–198, 1921.
- [2] G.R. Irwin, *Fracture, Elasticity and Plasticity*. Springer, Berlin, pp. 551–590, 1958.
- [3] F. Zhou and J.F. Molinari, Dynamic crack propagation with cohesive elements: A methodology to address mesh dependency, *Int. J. Numer. Meth. Engng.*, vol. 59, no. 1, pp. 1–24, 2004. DOI: [10.1002/nme.857](https://doi.org/10.1002/nme.857).
- [4] N.M. Azevedo and J.V. Lemos, Hybrid discrete element/finite element method for fracture analysis, *Comput. Methods Appl. Mech. Eng.*, vol. 195, no. 33–36, pp. 4579–4593, 2006. DOI: [10.1016/j.cma.2005.10.005](https://doi.org/10.1016/j.cma.2005.10.005).
- [5] C. Linder and F. Armiero, Finite elements with embedded branching, *Finite Elem. Anal. Des.*, vol. 45, no. 4, pp. 280–293, 2009. DOI: [10.1016/j.finel.2008.10.012](https://doi.org/10.1016/j.finel.2008.10.012).
- [6] I. Babuška, U. Banerjee, and J.E. Osborn, Generalized finite element methods - Main ideas, results and perspective, *Int. J. Comput. Methods*, vol. 01, no. 01, pp. 67–103, 2004. DOI: [10.1142/S0219876204000083](https://doi.org/10.1142/S0219876204000083).
- [7] N. Vu-Bac, H. Nguyen-Xuan, L. Chen, C.K. Lee, G. Zi, X. Zhuang, G.R. Liu, and T. Rabczuk, A phantom-node method with edge-based strain smoothing for linear elastic fracture mechanics, *J. Appl. Math.*, vol. 2013, pp. 1–12, 2013. DOI: [10.1155/2013/978026](https://doi.org/10.1155/2013/978026).
- [8] G.R. Johnson and R.A. Stryk, Eroding interface and improved tetrahedral element algorithms for high-velocity impact computations in three dimensions, *Int. J. Impact Eng.*, vol. 5, no. 1–4, pp. 411–421, 1987. DOI: [10.1016/0734-743X\(87\)90057-1](https://doi.org/10.1016/0734-743X(87)90057-1).
- [9] X.P. Xu and A. Needleman, Numerical simulations of fast crack growth in brittle solids, *J. Mech. Phys. Solids*, vol. 42, no. 9, pp. 1397–1434, 1994. DOI: [10.1016/0022-5096\(94\)90003-5](https://doi.org/10.1016/0022-5096(94)90003-5).
- [10] G.T. Camacho and M. Ortiz, Computational modelling of impact damage in brittle materials, *Int. J. Solids Struct.*, vol. 33, no. 20–22, pp. 2899–2938, 1996. DOI: [10.1016/0020-7683\(95\)00255-3](https://doi.org/10.1016/0020-7683(95)00255-3).
- [11] G.I. Barenblatt, The formation of equilibrium cracks during brittle fracture. General ideas and hypotheses. Axially-symmetric cracks, *J. Appl. Math. Mech.*, vol. 23, no. 3, pp. 444–622, 1959. DOI: [10.1016/0021-8928\(59\)90157-1](https://doi.org/10.1016/0021-8928(59)90157-1).
- [12] A. Hillerborg, M. Modéer, and P.E. Petersson, Analysis of crack formation and crack growth in concrete by means of fracture mechanics and finite elements, *Cem. Concr. Res.*, vol. 6, no. 6, pp. 773–781, 1976. DOI: [10.1016/0008-8846\(76\)90007-7](https://doi.org/10.1016/0008-8846(76)90007-7).
- [13] J.N. Reddy and A. Srinivasa, On the force-displacement characteristics of finite elements for elasticity and related problems, *Finite Elem. Anal. Des.*, vol. 104, pp. 35–40, 2015. DOI: [10.1016/j.finel.2015.04.011](https://doi.org/10.1016/j.finel.2015.04.011).
- [14] J.N. Reddy, *An Introduction to the Finite Element Method*, McGraw Hill, New York, 2006.
- [15] L.M. Kachanov, Time of the rupture process under creep conditions, *Izvestia Akademii Nauk SSSR, Otdelenie Tekhnicheskikh Nauk*, vol. 8, pp. 26–31, 1958.
- [16] Z.P. Bažant and B.H. Oh, Crack band theory for fracture of concrete, *Mat. Constr.*, vol. 16, no. 3, pp. 155–177, 1983. DOI: [10.1007/BF02486267](https://doi.org/10.1007/BF02486267).
- [17] G. Pijaudier-Cabot and Z.P. Bažant, Nonlocal damage theory, *J. Eng. Mech.*, vol. 113, no. 10, pp. 1512–1533, 1987. DOI: [10.1061/\(ASCE\)0733-9399\(1987\)113:10\(1512\)](https://doi.org/10.1061/(ASCE)0733-9399(1987)113:10(1512)).
- [18] A. Karamnejad, V.P. Nguyen, and L.J. Sluys, A multi-scale rate dependent crack model for quasi-brittle heterogeneous materials, *Eng. Fract. Mech.*, vol. 104, pp. 96–113, 2013. DOI: [10.1016/j.engfracmech.2013.03.009](https://doi.org/10.1016/j.engfracmech.2013.03.009).
- [19] L.F. Pereira, J. Weerheijm, and L.J. Sluys, A numerical study on crack branching in quasi-brittle materials with a new effective rate-dependent nonlocal damage model, *Eng. Fract. Mech.*, vol. 182, pp. 689–707, 2017. DOI: [10.1016/j.engfracmech.2017.06.019](https://doi.org/10.1016/j.engfracmech.2017.06.019).
- [20] J. Ožbolt, J. Bošnjak, and E. Sola, Dynamic fracture of concrete compact tension specimen: Experimental and numerical study, *Int. J. Solids Struct.*, vol. 50, no. 25–26, pp. 4270–4278, 2013. DOI: [10.1016/j.ijсолstr.2013.08.030](https://doi.org/10.1016/j.ijсолstr.2013.08.030).
- [21] S.A. Silling, Reformulation of elasticity theory for discontinuities and long-range forces, *J. Mech. Phys. Solids*, vol. 48, no. 1, pp. 175–209, 2000. DOI: [10.1016/S0022-5096\(99\)00029-0](https://doi.org/10.1016/S0022-5096(99)00029-0).
- [22] A. Pandolfi and M. Ortiz, An eigenerosion approach to brittle fracture, *Int. J. Numer. Meth. Engng.*, vol. 92, no. 8, pp. 694–714, 2012. DOI: [10.1002/nme.4352](https://doi.org/10.1002/nme.4352).
- [23] B. Schmidt, F. Fraternali, and M. Ortiz, Eigenfracture: An eigendeformation approach to variational fracture, *Multiscale Model. Simul.*, vol. 7, no. 3, pp. 1237–1266, 2009. DOI: [10.1137/08712568](https://doi.org/10.1137/08712568).
- [24] G. Francfort and J.J. Marigo, Revisiting brittle fracture as an energy minimization problem, *J. Mech. Phys. Solids*, vol. 46, no. 8, pp. 1319–1342, 1998. DOI: [10.1016/S0022-5096\(98\)00034-9](https://doi.org/10.1016/S0022-5096(98)00034-9).
- [25] G. Dal Maso and R. Toader, A model for the quasi-static growth of brittle fractures: Existence and approximation results, *Arch. Ration. Mech. Anal.*, vol. 162, no. 2, pp. 101–135, 2002.
- [26] B. Bourdin, G. Francfort, and J.J. Marigo, Numerical experiments in revisited brittle fracture, *J. Mech. Phys. Solids*, vol. 48, no. 4, pp. 797–826, 2000. DOI: [10.1016/S0022-5096\(99\)00028-9](https://doi.org/10.1016/S0022-5096(99)00028-9).
- [27] B. Bourdin, C.J. Larsen, and C. Richardson, A time-discrete model for dynamic fracture based on crack regularization, *Int. J. Fract.*, vol. 168, no. 2, pp. 133–143, 2011. DOI: [10.1007/s10704-010-9562-x](https://doi.org/10.1007/s10704-010-9562-x).
- [28] M.J. Borden, C.V. Verhoosel, M.A. Scott, T.J.R. Hughes, and C.M. Landis, A phase-field description of dynamic brittle fracture, *Comput. Methods Appl. Mech. Eng.*, vol. 217–220, pp. 77–95, 2012. DOI: [10.1016/j.cma.2012.01.008](https://doi.org/10.1016/j.cma.2012.01.008).
- [29] A. Schlüter, A. Willenbücher, C. Kuhn, and R. Müller, Phase field approximation of dynamic brittle fracture, *Comput. Mech.*, vol. 54, no. 5, pp. 1141–1161, 2014. DOI: [10.1007/s00466-014-1045-x](https://doi.org/10.1007/s00466-014-1045-x).
- [30] G. Liu, Q. Li, M.A. Msekh, and Z. Zuo, Abaqus implementation of monolithic and staggered schemes for quasi-static and dynamic fracture phase-field model, *Comput. Mater. Sci.*, vol. 121, pp. 35–47, 2016. DOI: [10.1016/j.commatsci.2016.04.009](https://doi.org/10.1016/j.commatsci.2016.04.009).
- [31] S. Li, L. Tian, and X. Cui, Phase field crack model with diffuse description for fracture problem and implementation in engineering applications, *Adv. Eng. Softw.*, vol. 129, pp. 44–56, 2019. DOI: [10.1016/j.advengsoft.2018.09.005](https://doi.org/10.1016/j.advengsoft.2018.09.005).
- [32] M.J. Borden, T.J. Hughes, C.M. Landis, and C.V. Verhoosel, A higher-order phase-field model for brittle fracture: Formulation and analysis within the isogeometric analysis framework, *Comput. Methods Appl. Mech. Eng.*, vol. 273, pp. 100–118, 2014. DOI: [10.1016/j.cma.2014.01.016](https://doi.org/10.1016/j.cma.2014.01.016).
- [33] C.V. Verhoosel and R. Borst, A phase-field model for cohesive fracture, *Int. J. Numer. Meth. Engng.*, vol. 96, no. 1, pp. 43–62, 2013. DOI: [10.1002/nme.4553](https://doi.org/10.1002/nme.4553).
- [34] D. Kamensky, G. Moutsanidis, and Y. Bazilevs, Hyperbolic phase field modeling of brittle fracture: Part I-theory and simulations, *J. Mech. Phys. Solids*, vol. 121, pp. 81–98, 2018. DOI: [10.1016/j.jmps.2018.07.010](https://doi.org/10.1016/j.jmps.2018.07.010).
- [35] L. Hai, J.-Y. Wu, and J. Li, A phase-field damage model with micro inertia effect for the dynamic fracture of quasi-brittle solids, *Eng. Fract. Mech.*, vol. 225, pp. 106821, 2020. DOI: [10.1016/j.engfracmech.2019.106821](https://doi.org/10.1016/j.engfracmech.2019.106821).
- [36] C. Miehe, M. Hofacker, and F. Welschinger, A phase field model for rate-independent crack propagation: Robust algorithmic implementation based on operator splits, *Comput. Methods Appl. Mech. Eng.*, vol. 199, no. 45–48, pp. 2765–2778, 2010. DOI: [10.1016/j.cma.2010.04.011](https://doi.org/10.1016/j.cma.2010.04.011).